COMPARATIVE ANALYSYS BY FINITE ELEMENT METHOD OF WELDING PATHS IN ALUMINIUM ALLOYS T-JOINTS

M. C. Gheonea, G. Simion*, D. C. Birsan, L. R. Mistodie,
B. Georgescu, C. C. Rusu, E. Scutelnicu

"Dunarea de Jos" University of Galati, Centre for Advanced Research in Welding,
Faculty of Engineering, Romania
47 Domneasca St., 800008 – Galati, Tel. +40336130208
*Corresponding author's e-mail address: george.simion@ugal.ro

ABSTRACT

In recent decades, due to their great advantages, the aluminium alloys have been more and more used in the shipbuilding industry, particularly in the construction of yacht superstructures. Nevertheless, a significant disadvantage of aluminium alloys subjected to welding is their high deformation tendency, which represents an important drawback that needs additional remedial measures. In this study, a finite element analysis was performed, in order to investigate and optimize the design of welding paths used to carry out AA 5083 aluminium alloy T-joints of 6mm thick sheets by Metal Inert Gas (MIG) welding. The research methodology was focused on three case studies, in order to determine and comparatively analyse the Heat Affected Zone extend and the level of stress and displacement. In the first case, the welding beads were successively deposited, following the same welding direction. In the second case, the seams were successively welded, but the welding directions on one side and on the other side of the joint were opposite. In the third case, the seams were simultaneously welded, on both sides of the joint, the welding directions being opposite, as in the previous case study. Based on the research results, it was found that the larger Heat Affected Zone (HAZ) was identified in the third case study, while the total displacement was 25-30% lower, in comparison with the results obtained in the first two case studies. This phenomenon can be explained by the high amount of heat developed simultaneously by two electric arcs and transferred, by conduction, to the base materials. Due to the joining technology applied, that consisted in welding simultaneously on both sides of the joint, an adequate balance of stress and strain was achieved, determining a lower total displacement.

KEYWORDS: *finite element analysis, AA5083 T-joint, welding paths, equivalent stresses, heat affected zone, total displacements*

1. INTRODUCTION

Aluminium-based alloys are widely acknowledged for their exceptional properties, including high machinability, low density, significant mechanical strength, and superior corrosion resistance. These attributes make them highly suitable for a wide spectrum of industrial applications, particularly in the construction of river and marine vessels, as well as offshore infrastructures. Among the various range of aluminium alloys, those belonging to the 5xxx and 6xxx series are especially valued for their optimal balance of mechanical strength, corrosion resistance, and weldability. These characteristics facilitates the design and fabrication in shipbuilding industry, for hull structures, superstructures, and deck assemblies.

The use of aluminium alloys in these particular components enables the design of vessels with enhanced performance capabilities, including increased speed, greater cargo capacity, and reduced maintenance requirements, thereby contributing to overall operational efficiency and cost-effectiveness [1-8].

In the field of shipbuilding, fusion welding is considered to be the predominant method for joining aluminium alloy components. This welding process is preferred due to its capacity to produce joints with favourable mechanical properties, reduced mass, excellent seal integrity, and appropriateness for automation and robotisation applications. The most critical physical property, influencing the weldability of aluminium alloys, is the thermal conductivity, which

is approximately four times greater that of other materials, as steel. As a result, to achieve the same local temperature increase in aluminium, as in steels, necessitates a fourfold acceleration in heat input. This elevated thermal conductivity, while presenting challenges in temperature management, also offers the advantage of a rapid solidification of the molten metal, facilitating welding in complex positions. Moreover, the welding of aluminium alloys is challenging by the formation of an oxide layer (primarily aluminium oxide, Al_2O_3) on their surfaces upon exposure to air. This oxide layer has a higher melting point (approximately 2072°C) compared to the aluminium, potentially leading to welding defects such as lack of fusion, porosity, and reduced ductility. To ensure defect-free welds, this oxide layer must be meticulously removed prior to welding, through mechanical methods such as machining, filing, wire brushing, or chemical cleaning. For the welding technologies applied to shipbuilding, cathodic cleaning serves as an alternative approach for oxide removal. This method can be achieved via Direct Current Metal Inert Gas (DC-MIG) welding with the electrode wire as the positive pole or by employing Alternating Current Tungsten Inert Gas (AC-TIG) welding. The removal of aluminium oxides is critical, as their entrapment in the weld seam can compromise joint integrity, leading to cracking and diminished structural performance. During welding, preventing re-formation of the oxide layer is achieved by shielding the weld zone with fluxes or employing inert gases such as argon, helium, or hydrogen [9-15].

Another critical aspect during the welding of aluminium alloys is their susceptibility to deformation. Thermal expansion and contraction during welding can lead to warping, which not only affects the aesthetic quality of the weld but also its structural integrity [16-18]. This is particularly noticeable in T-joint configurations, which are commonly used in shipbuilding structures fabrication. The thermal stresses induced by welding often result in deformation of the joints, potentially undermining the vessel's durability and safety [19-22].

Finite Element Method (FEM) is a powerful computational technique that enables the modelling and simulation of heat transfer, stress and strains prediction, providing analytical insights for determining optimal welding sequence and appropriate welding parameters, in order to minimize distortions and enhance the quality of the joints. Many researches focused on different techniques for the modelling and simulation of the heat transfer and distortions prediction. In most of the cases, particular conclusions were drawn, but methodologies of the design of welding paths requires still to be determined [23-26].

In this respect, in the present study, FEM is employed to investigate the influence of the welding paths on the stress and strain levels, in case of a 5xxx series aluminium alloy T-joint. The analysis aims to optimize welding strategies to ensure a structural reliability and minimize post-weld corrective measures.

2. MATERIALS AND METHODS

2.1. Materials and Methods

To conduct the numerical simulation of the welding process, a geometric model of a T-joint configuration was developed. This model consists of two aluminium plates with dimensions of 500 mm × 600 mm and 500 mm × 300 mm, respectively, each with a thickness of 6 mm, as illustrated in figure 1. The chemical composition of the AA5083 aluminium alloy used in the analysis is detailed in table 1, while its mechanical properties, including yield strength, ultimate tensile strength, and elongation at break, are presented in Table 2.

The simulated welding process was the Metal Inert Gas (MIG), with the welding parameters shown in table 3. These parameters were carefully selected, reflecting industrial welding procedures, and ensuring the simulation fidelity. The relatively higher heat input associated with these parameters is required when welding aluminium alloys to compensate for their enhanced heat dissipation characteristics.
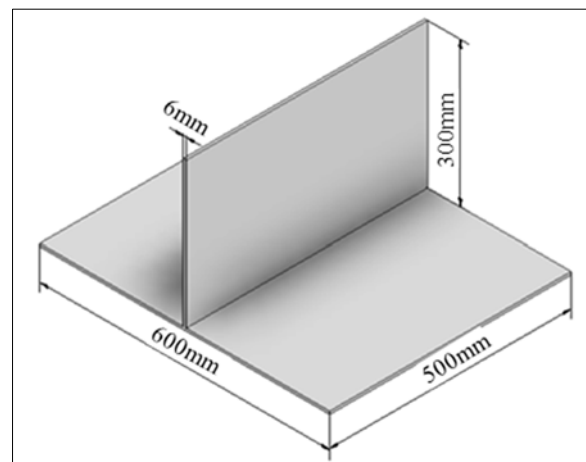

Fig. 1. Schematic representation of the T joint

The primary objective of this study was to analyse three distinct case studies for the bilateral welding of the T-joint and determine which welding sequence results in the lowest equivalent stress and displacement values. The three welding strategies investigated are depicted in figure 2 and are described as follows:

- Case Study 1 (Fig. 2a): Welding beads 1 and 2 are deposited successively, both starting from the same side of the joint.
- Case Study 2 (Fig. 2b): The welding beads are also deposited successively; however, the process begins from opposite sides of the joint, promoting a counterbalanced heat distribution.

- Case Study 3 (Fig. 2c): Both welding beads are deposited simultaneously, initiating from opposite sides of the joint, to assess the impact of concurrent heat input on residual stress and distortion.

For the sake of clarity and conciseness, the three configurations will henceforth be referred to as Case 1, Case 2, and Case 3 in the subsequent analysis.
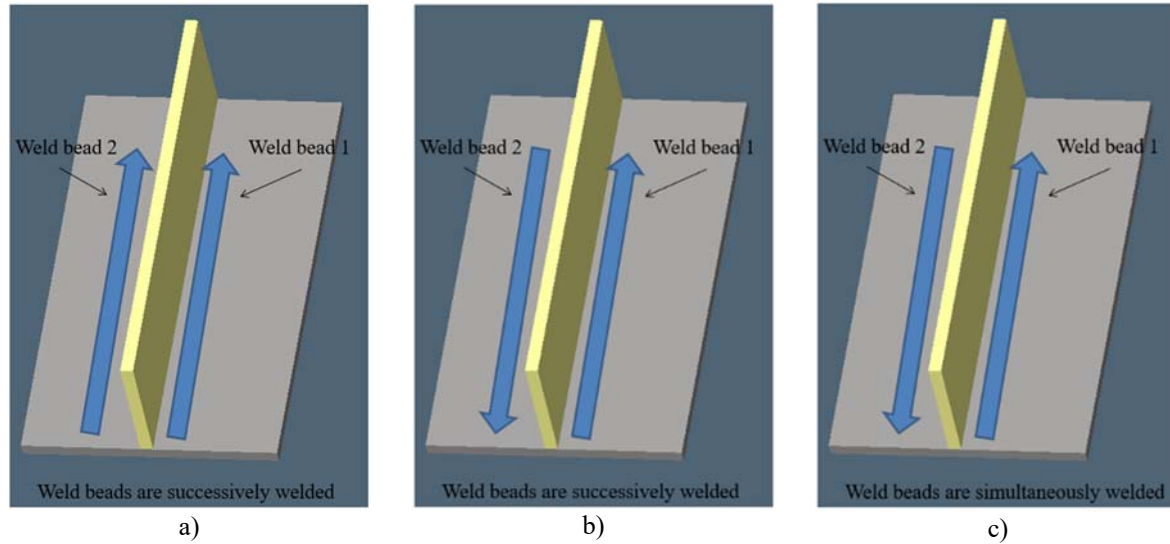

a)   b)   c)

Fig. 2. Schematic representation of the weld bead paths

Table 1. Chemical composition of 5083 Al alloy [wt%]

Cr	Cu	Fe	Mg	Mn	Si	Ti	Zn	Al
0.15	0.1	0.4	4.5	0.7	0.4	0.15	0.25	Bal.

Table 2. Mechanical characteristics of 5083 Al Alloy

Tensile Strength, Yield [MPa]	Tensile Strength, Ultimate [MPa]	Elongation [%]
228	317	23

Table 3. Welding parameters

Current [A]	Voltage [V]	Travel speed [cm/min]	Heat input [J/cm]
120	23	50	3284

2.2. Geometric Model

The geometric model required for this analysis was designed using MSC Apex software, a leading solution in the domain of computer-aided engineering (CAE) for geometric modelling and meshing. The finite element analysis (FEA) simulation was performed with Simufact Welding, a specialized simulation environment designed for modelling welding processes, thermal cycles, and resulting distortions. Both software licenses are provided by the Centre for Advanced Research in Welding (SUDAV) within the Faculty of Engineering at the "Dunarea de Jos" University of Galati.

The model comprises a total of 412160 elements and 95992 nodes for the aluminium plates, and 10200 elements along with 14248 nodes for the weld beads. The element type used for meshing is the tetrahedral element, which is well-suited for capturing complex geometries and thermal gradients. To enhance the accuracy of the simulation and optimize computational efficiency, the mesh was locally refined along the welding paths. The boundary conditions and the meshed geometric model is illustrated in figure 3.
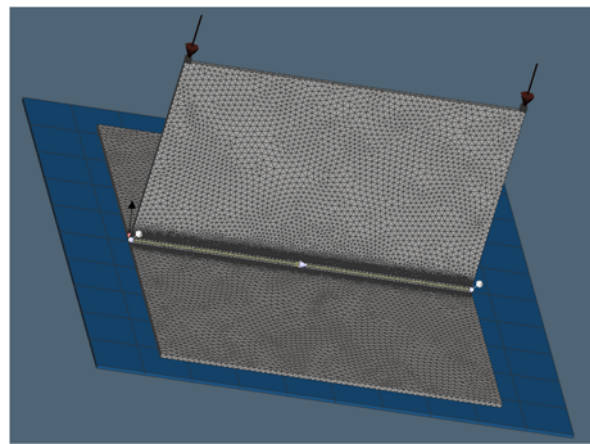

Fig. 3. Finite element model of the 5083 Al alloy welded joint

The simulation employed a volumetric semi-ellipsoidal heat source, based on the Goldak double-ellipsoidal model, which is widely recognized for its ability to replicate the distribution of heat during welding with high fidelity.
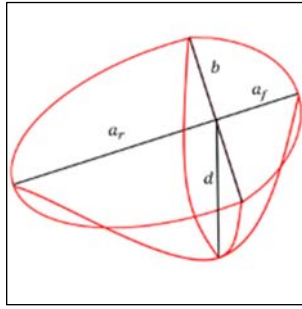
Fig. 4. Heat source model of the AA 5083 welded joint

As represented in figure 4, the parameters defining the semi-ellipsoid, which were estimated by the

Simufact Welding software, based on the welding parameters, are as follows:

- a_f (front length): 2.3 mm;
- a_r (rear length): 9.2 mm;
- b (width): 2.8 mm;
- d (depth): 5.8 mm.

The variation of thermo-physical and mechanical characteristics depending on temperature were taken into account, these being available in the database of the Simufact Welding program. In figure 5a, b and c are presented the thermo-physical and mechanical characteristics depending on temperature, respectively the thermal conductivity, specific heat, Young's and in the figure 5d the effective plastic strain depending on the flow stress.
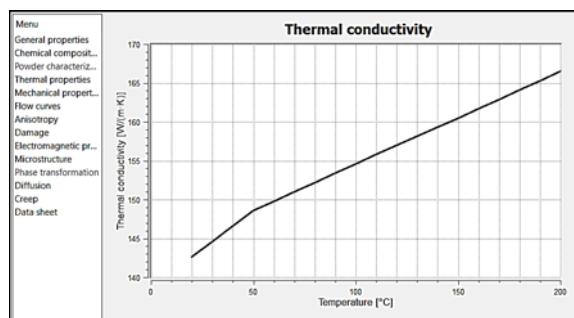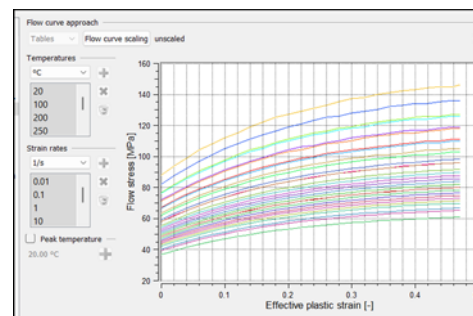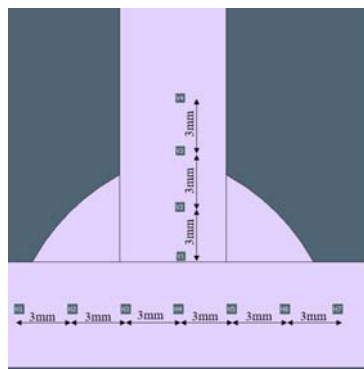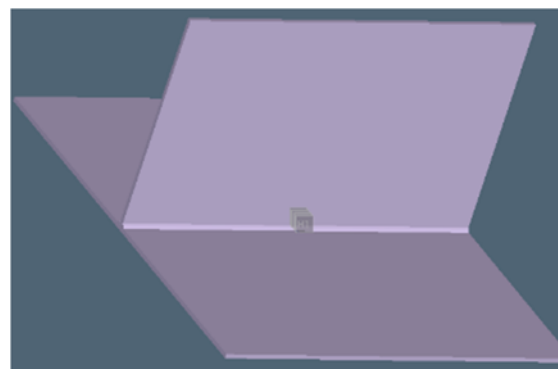

a)
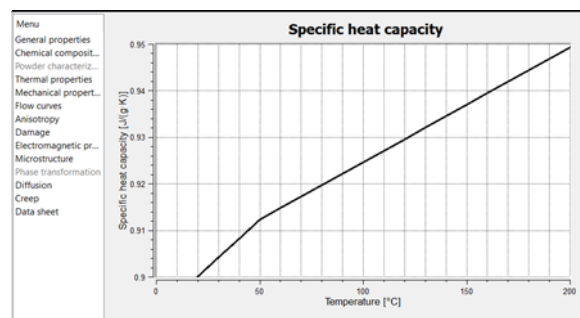
b)
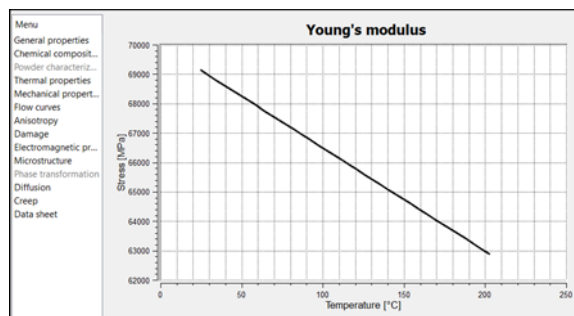
c)

d)

Fig. 5. Thermo-physical and mechanical characteristics of AA5083

a)

b)

Fig. 6. Analysed nodes in the FEM analysis

To achieve a comprehensive understanding of the thermal and mechanical phenomena that occurs during the welding process, data collection points were strategically positioned within the plates. These points were positioned at the mid-thickness (Fig. 6.a) and mid-length (Fig. 6.b) of each plate in order to capture the associated thermal gradients and mechanical responses both during and following the welding process. The spacing between the selected nodes was set at 3 mm, providing adequate resolution for identifying zones of stress concentration and displacement patterns. The gathered data facilitated the evaluation of equivalent stress distributions, thermal profiles, and residual deformations under different welding sequences. This information is important for optimizing welding strategies in order to minimize warping and improve joint integrity in naval and offshore applications.

3. RESULTS AND DISCUSSION

3.1. Temperature Field

The temperature field distribution during the welding process describes the spatial distribution of temperatures within the welded assembly, reflecting the thermal gradients induced by the introduced heat input. Understanding the temperature field distribution is important for predicting and analysing several welding-induced phenomena, such as equivalent stress, displacement, and microstructural transformations within the welded joint [27].

In the figure 7 are presented the resulted temperature fields for the three analysed welding configurations (Case 1, Case 2, and Case 3). Due to the high thermal conductivity of the 5083-aluminium alloy, the propagation of the temperature within the welded joint components is relatively constrained. This rapid heat dissipation, characteristic of aluminium alloys, results in more localized temperature elevations compared to other materials, with lower thermal conductivity.

In Case 1 and Case 2, the 185°C isotherm of the first weld bead is situated at approximately 12 mm from the centre of the melted welding pool. This limited thermal extension is indicative of effective heat dispersion. In contrast, in Case 3, where both weld beads are deposited simultaneously from opposite sides of the vertical plate, the 185°C isotherm extends 50% further into the joint, reaching a distance of approximately 19 mm. This extension results from the superimposition of two heat sources, which concentrate thermal energy at the joint's centreline, due to the close proximity of the bead paths. Such localized thermal increase can significantly affect the microstructural stability and potential residual stresses development in the region.

To gain deeper insights into the thermal behaviour during welding, the thermal history of specific nodes, located within both the vertical and horizontal plates, was monitored. These nodes were strategically positioned at the mid-thickness and mid-length of each plate to accurately capture the temperature evolution during welding (Fig. 8). For the vertical plate, Case 1 and Case 2 exhibit two distinct temperature peaks, corresponding to the sequential passage of the heat source during the welding of bead 1 followed by bead 2 (Fig. 8a and Fig. 8b). The maximum temperature attained in the middle of the vertical plate's thickness is approximately 400–420°C, at nodes V1 and V2.

However, at node V4, located 9 mm from the centre of the welded joint, the temperature decreases by nearly 30%, reaching values of 270–290°C. This temperature drop signifies effective lateral heat dissipation away from the weld zone. Furthermore, the thermal analysis indicates that in Case 1 and Case 2, the temperature does not reach the melting point of aluminium alloy (~600°C) at the mid-thickness of the vertical plate, implying that full penetration is not achieved in these welding configurations. In contrast, Case 3, which involves simultaneous welding of the two beads deposited from opposite sides, and where heat sources pass one near each other in the middle of the welded joint, significantly higher temperatures are achieved at the same nodes. The thermal history of nodes V1, V2, and V3 illustrates that the temperature exceeds the melting point, indicating complete weld penetration in this configuration (Fig. 8c).
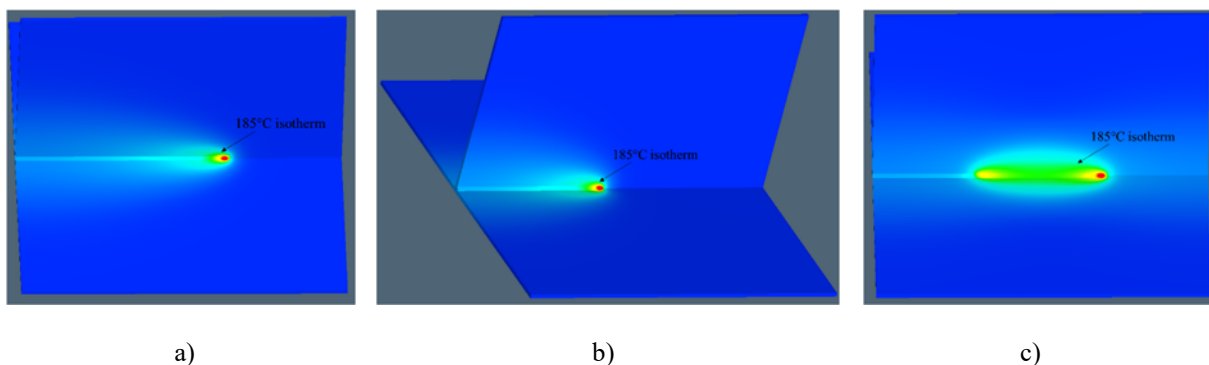

a)   b)   c)

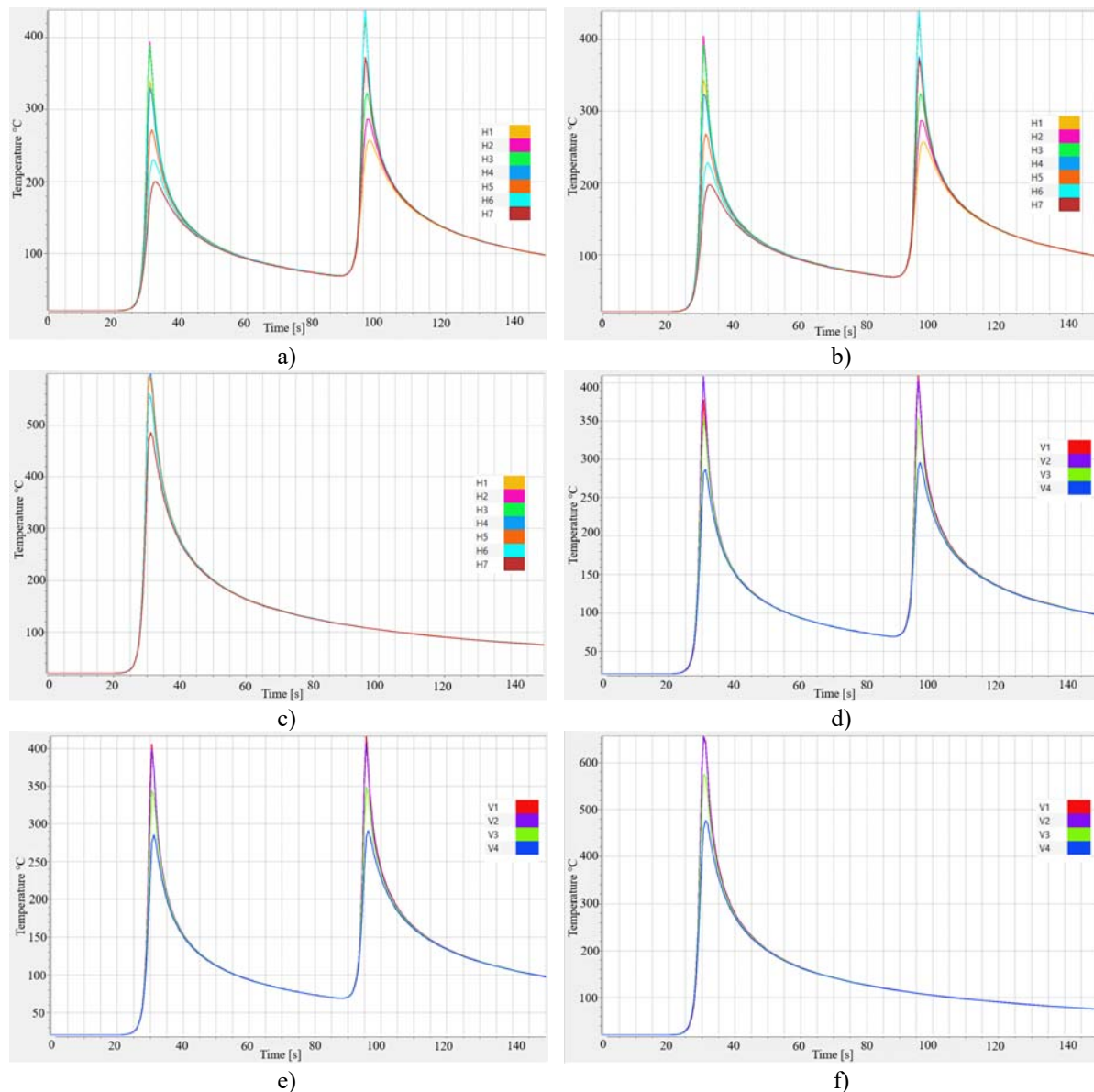**Fig. 7.** Temperature fields for Case Studies 1, 2 and 3

Fig. 8. Thermal history in the selected nodes: a) vertical plate Case 1; b) vertical plate Case 2; c) vertical plate Case 3; d) horizontal plate Case 1; e) horizontal plate Case 2; f) horizontal plate Case 3

A similar behaviour is observed in the horizontal plate, where the thermal history reflects two temperature peaks for Case 1 and Case 2, corresponding to the deposition of the two welding beads. In these cases, the maximum temperature at nodes H2 and H3, located adjacent to weld bead 1, does not exceed 400°C, which is slightly lower than the temperatures observed in the vertical plate (Fig. 8d, e, and f). This discrepancy is attributed to the greater mass and surface area of the horizontal plate, which enhances its capacity to dissipate heat. However, at nodes H5 and H6, positioned near weld bead 2, the maximum temperatures increase to approximately 420–440°C. This elevation is explained by the preheating effect induced by the prior welding of Bead 1. In Case 3, the thermal profile shows a single dominant peak at nodes H3, H4, and H5, where

temperatures exceed the melting point, mirroring the behaviour observed in the vertical plate.

The analysis of the temperature field distribution also allows the estimation of the Heat-Affected Zone (HAZ), which is the region around the weld that experiences microstructural changes due to exposure to high temperatures [28-30]. Figure 9 depicts the HAZ expansion for the three case studies, highlighting regions where the temperature surpasses the critical threshold required for HAZ formation. In Case 1 and Case 2, during the welding of the first bead, the HAZ extends approximately 7mm into the vertical plate and 11mm into the horizontal plate (Fig. 9a, and c). The preheating effect induced by the first bead increases the thermal exposure during the welding of the second bead, expanding the HAZ in the horizontal plate by approximately 30%, reaching a total width of 15mm (Fig. 9b, and d).

For Case 3, the simultaneous deposition of the weld beads generates the most extensive HAZ, with a maximum expansion of 16mm in the vertical plate and 33mm in the horizontal plate at the centre of the welded joint, where the beads pass one near each other, and where the peak temperature is reached (Fig. 9e). However, as the trajectory progresses towards the periphery of the welded joint, the HAZ width diminishes to around 7–8mm in the vertical plate at a distance of 125mm from the edge.

Additionally, a noticeable asymmetry in the HAZ extension in the horizontal plate is observed, influenced by the preheating effect. When the first weld bead reaches the 125mm reference point, the HAZ measures 13mm. Upon the arrival of the second weld bead, the HAZ further expands to 18mm, demonstrating the cumulative thermal impact of successive welding passes.
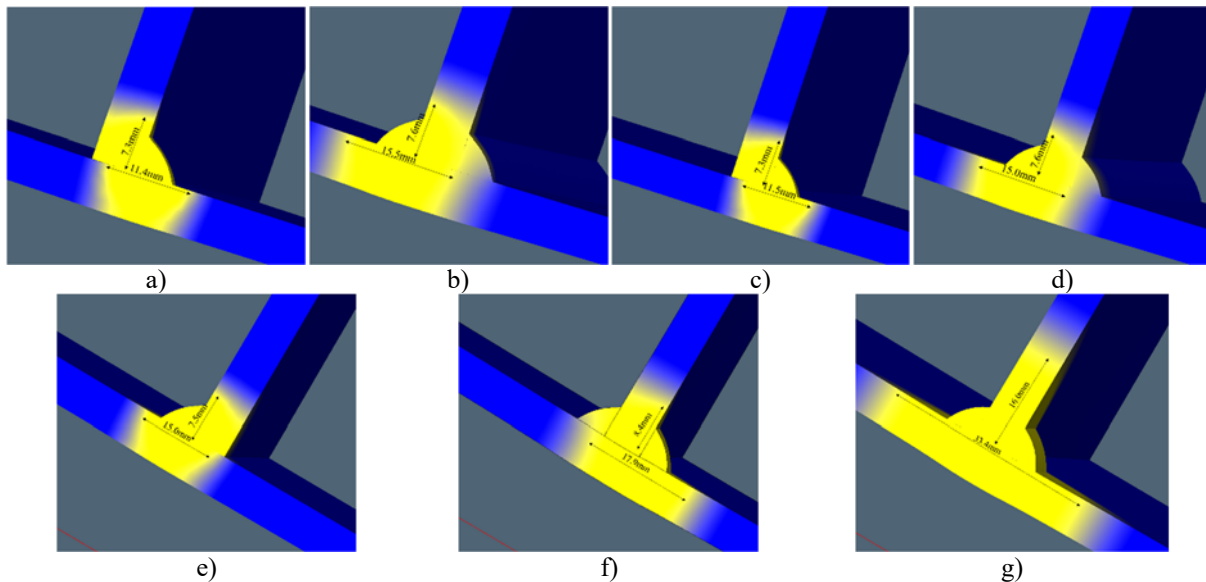

a)   b)   c)   d)

e)   f)   g)

Fig. 9. Extension of the HAZ: a) first bead Case 1; b) second bead Case 1; c) first bead Case 2; d) second bead Case 2; e) middle of the joint Case 3; f) first bead Case 3; g) second bead Case 3

3.2. Stresses Distribution

The stress distribution that develops during the welding process is the result of a complex interaction of several factors. The ones that have the most influence among these are the non-uniform heating and cooling cycles experienced by the welded material.

When subjected to localized heat input from the welding source, the material near the weld pool expands rapidly, while the surrounding cooler regions remain relatively stable. This thermal gradient induces thermal stresses due to constrained expansion.

Upon cooling, the welded material contracts unevenly, leading to the development of residual stresses. The severity of these stresses is further influenced in multi-pass welding, where repeated thermal cycles exacerbate expansion and contraction phenomena, increasing the potential for distortion and residual stress buildup. Figure 10 illustrates the equivalent (von Mises) stress distributions for the three welding configurations (Case 1, Case 2, and Case 3). The simulation results indicate that the maximum equivalent stresses are concentrated predominantly around the weld beads, with stress magnitudes ranging from 170 MPa to 180 MPa, across all case studies. Despite the overall similarity in peak stress values, a

noteworthy observation is noted in Case 3 (Fig. 10c), where the area of maximum stress concentration is nearly double in size at the centre of the welded joint compared to Case 1 and Case 2 (Fig. 10a, and b).

This phenomenon is attributed to the simultaneous welding of both beads from opposite sides, resulting in a higher localized temperature and a more extended Heat-Affected Zone (HAZ), as previously observed in the temperature field analysis.

Figure 11 presents the evolution of equivalent stresses at the selected nodes within both the horizontal and vertical plates. This temporal analysis provides insights into the dynamic stress fluctuations induced by the welding process.

In figure 11a and figure 11b, the horizontal plate's stress development for Case 1 and Case 2 is depicted. The stress values at nodes H1-H4 show an initial rise to approximately 100-110MPa around the second 30 of the simulation process, correlating with the arrival of the welding arc at the monitored nodes. As the heat source remains in proximity, minor fluctuations in stress are observed, followed by a gradual increase to around 170 MPa at the nodes positioned adjacent to the welded bead (H1-H4). As observed in figure 10, the maximum stresses in the welded joint developed in this area, near the welding beads.
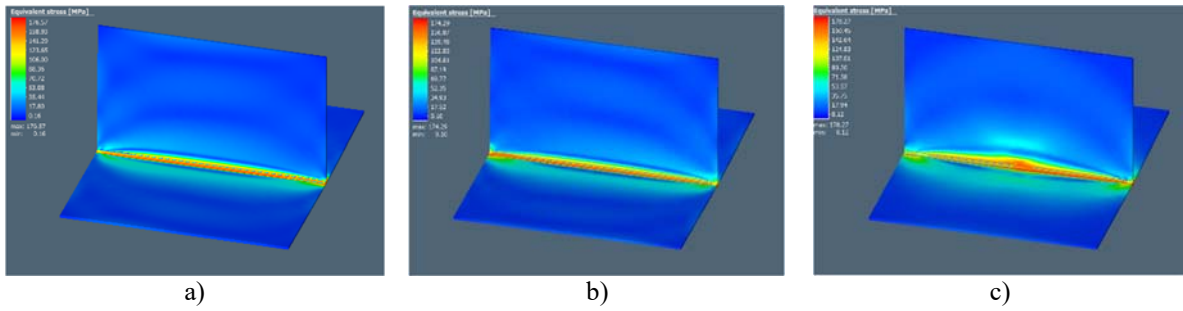
Fig. 10. Stress development during welding: a) Case Study 1; b) Case Study 2; c) Case Study 3
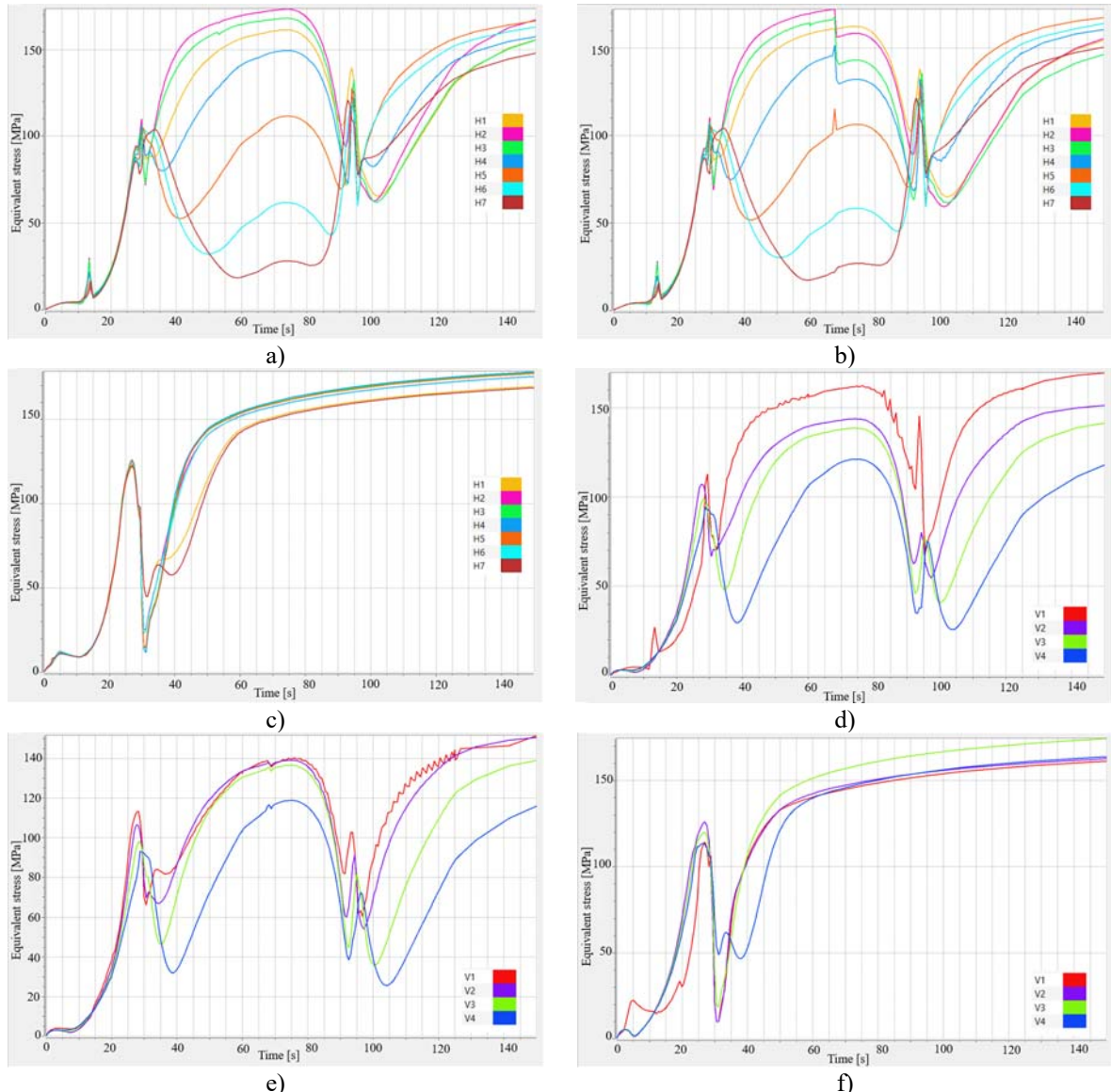

Fig. 11. Equivalent stress-time variation during welding: a) horizontal plate Case 1; b) horizontal plate Case 2; c) horizontal plate Case 3; d) vertical plate case1; e) vertical plate case 2; f) vertical plate case 3

On the opposite side of the vertical plate, the stress levels at nodes H5-H7 exhibit a gradual decrease as the distance from the weld centre increases, reaching values below 50MPa. This drop reflects the attenuation of thermal gradients with increasing distance from the weld line. However, upon the initiation of the second welding pass, around second 90, when the second bead reaches the nodes, a decrease in the stresses is observed again, up to about 100MPa, in the nodes where the stresses exceed this value, and, once the heat source moves forward, a secondary surge in equivalent stress is observed, peaking again at around 170MPa near the welded regions.

Notably, after the completion of the second bead, the stress values across all nodes become more uniform, with reduced variation compared to the initial welding phase. This homogenization occurs because the vertical plate becomes securely welded to the horizontal plate on both sides, creating a more balanced load distribution and reducing differential contraction stresses.

In figure 11c, the equivalent stress history for Case 3 demonstrates a distinct behaviour. Stress values rise to approximately 120 MPa by the 30-second mark, coinciding with the simultaneous arrival of the two welding arcs at the joint's centre. Unlike Cases 1 and 2, the stress levels in the central nodes (H3-H5) experience a sharp and abrupt decline to around 10MPa. This dramatic decrease is explained by the complete penetration achieved in this area in Case 3, as observed in the temperature field analysis. The simultaneous welding leads to localized melting and stress relief in the central region, which is not achieved in the other two cases.

As the heat sources move away from the central area, stress values increase steadily to approximately 170–180MPa, reflecting the material's contraction and solidification. Moreover, figure 11 a, b, and c illustrate that in Case 3, the stress distribution across the selected nodes is more uniform, with considerably smaller deviations compared to Case 1 and Case 2, where differences of up to 100 MPa in the selected nodes were noted. This uniformity is indicative of more balanced thermal and mechanical load distribution during the welding sequence.

The temporal evolution of equivalent stress in the vertical plate is depicted in figure 11 d, e, f. A similar trend to the horizontal plate is observed, with stress values peaking around 170–180 MPa. The rise and fall of stress values correspond directly to the proximity of the welding arc in the analysed nodes. The maximum stress values remain relatively consistent across all three welding scenarios; however, the rate of change and uniformity differ notably in Case 3 due to the simultaneous welding of the beads starting form opposite sides.

3.3. Displacements

The study of displacements resulting from welding processes is important for ensuring the quality, structural integrity, and functional performance of welded joints. Displacements can introduce a range of structural issues, including misalignment of components, which leads to a complicate assembly process and compromises the ability to meet design tolerances. Furthermore, excessive deformations often require expensive corrective measures, such as mechanical straightening or machining, in order to restore the welded structure to its intended geometric specifications. Therefore, both production costs and manufacturing time will increase. In structural applications, particularly those involving aesthetic considerations, such as decorative panels or visible maritime structures, significant distortions can degrade the visual appearance and compromise design specifications. Thus, controlling welding-induced displacements is critical for achieving both functional and aesthetic requirements in industrial applications.

Figure 12 illustrates the total displacement fields for the three welding configurations analysed (Case 1, Case 2, and Case 3). The simulation results reveal that the maximum displacement values are concentrated primarily at the edges of the horizontal plate. This region is particularly susceptible to deformation due to its unsupported length and its exposure to thermal gradients during the welding process.

In Case 1 and Case 2, the maximum displacements are observed to reach approximately 10 mm and 11.5 mm, respectively. These displacements are concentrated in the section of the horizontal plate, where the second weld bead is deposited. The additional, thermal input during the second pass leads to further expansion and contraction, thereby amplifying the overall deformation. In Case 3, where simultaneous bilateral welding is performed, the total displacements are reduced by approximately 20–25%, achieving a maximum displacement of 8.6 mm. This decrease is due to the simultaneous thermal loading, which permits a more symmetric heat distribution, thereby mitigating the uneven thermal expansion. The variation of displacements in the specific selected nodes for the analysis is presented in figure 13. Although the displacement values in these points are relatively minor, generally not exceeding 1 mm, due to their proximity to the weld bead, the displacement profiles offer valuable insights into the dynamic behaviour of the welded joint, during the thermal cycles.

In Cases 1 and 2 (Fig. 13a and b), the displacement evolution is characterized by a gradual increase to approximately 0.2 mm up to the 30-second mark, corresponding to the arrival of the welding arc onto selected nodes. This period is marked by localized thermal expansion, leading to an incremental displacement accumulation. When the heat source moves beyond the nodes, a slight fluctuation in displacement occurs, followed by a secondary increase, up to around 0.3 mm. The displacements remain relatively constant until around 90 seconds, when the second weld bead is deposited. This additional pass induces a renewed expansion with maximum displacement values of 0.6–0.7 mm, recorded at node H7, located in the horizontal plate adjacent to the site of the second bead. This behaviour highlights the cumulative successive thermal effects from the multi-pass welding, which induces further plastic deformation in the joint.

For Case 3 (Fig. 13c), where both weld beads are deposited simultaneously, from opposite sides, the displacements show a more controlled and symmetric distribution. The values increase gradually up to 0.3mm, as the two heat sources converge to the joint's

centre. At this point, minor fluctuations are observed, with displacements stabilized within a range of 0.1-0.4mm, with the lowest values recorded in node H4. This uniformity is indicative of the balanced thermal input characteristic of the simultaneous welding strategy, which reduces the tendency for uneven expansion and contraction. Similar displacement patterns are visible in the vertical plate across all three case studies (Fig. 13d, e and f). Displacement values follow a cyclic increase and decrease, as the welding arc approaches and moves away from the analysed nodes. The maximum displacements in this region reach up to 0.5–0.7mm.
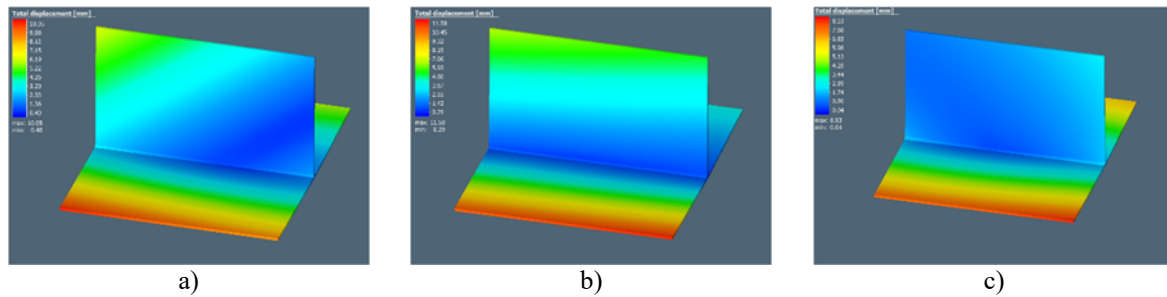

a)   b)   c)

Fig. 12. Total displacement development during welding a) Case Study 1; b) Case Study 2; c) Case Study 3
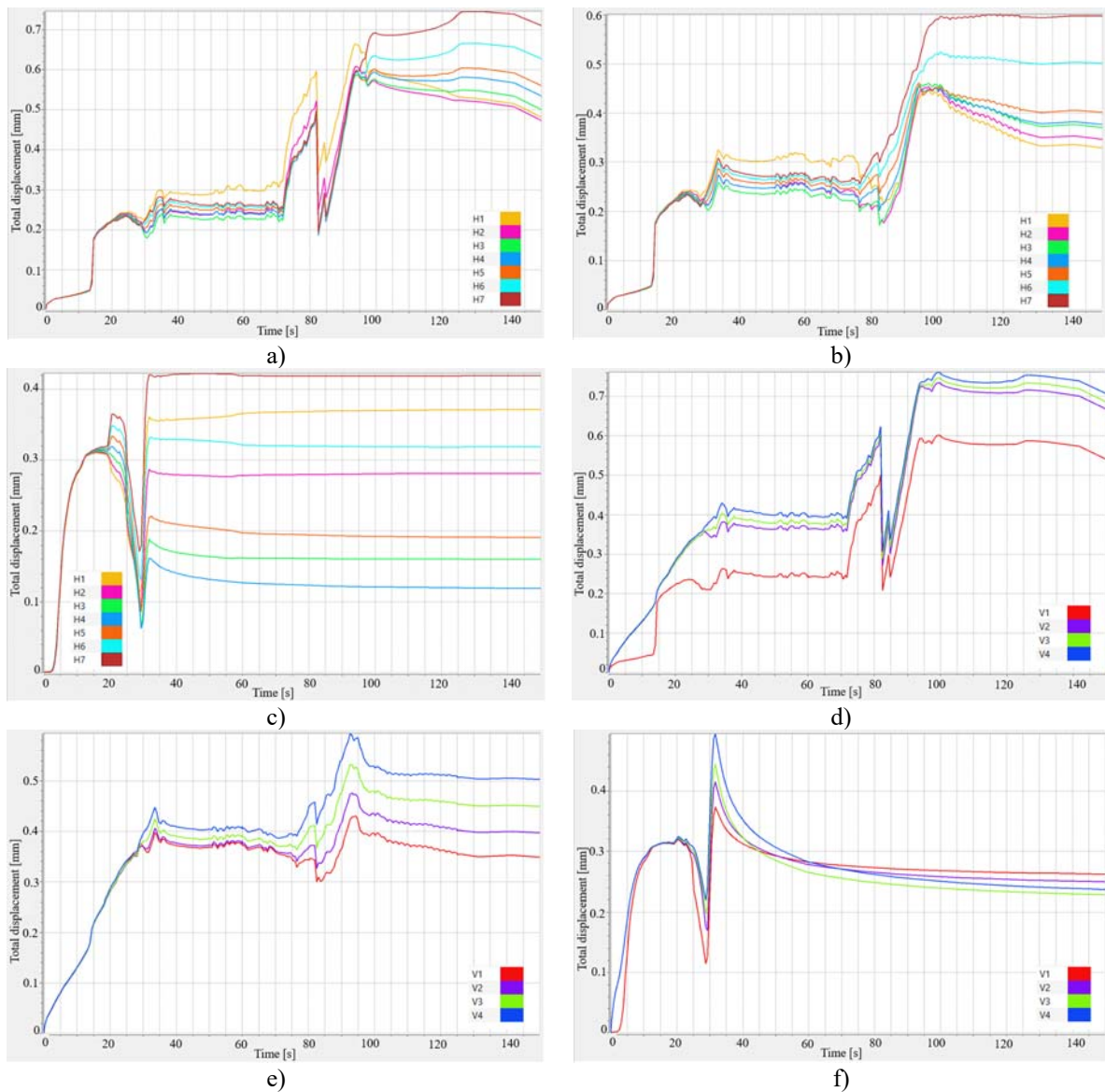

a)   b)

c)   d)

e)   f)

Fig. 13. Total displacement-time variation during welding a) horizontal plate case1; b) horizontal plate case 2; c) horizontal plate case 3; d) vertical plate case1; e) vertical plate case 2; f) vertical plate case 3

The significant reduction in total displacement observed in Case 3 can be attributed of two primary factors:

- *reduced exposure time to non-uniform heating*. In Case 3, the welding process concludes 60 seconds earlier than in Cases 1 and 2, as both beads are deposited simultaneously rather than sequentially. Consequently, the welded joint experiences less cumulative thermal effects, minimizing the potential for excessive thermal expansion and contraction. The displacement profile in figure 12c and f confirms this behaviour, where deformations stabilize after 30 seconds, while in Cases 1 and 2 (Fig. 13a, b, d, and e), additional deformation is observed, at the 90-second mark, because of the influence of the second weld bead deposition.

- *uniform stress distribution*: The balanced stress profiles observed in Case 3 (Figure 11c, and d) further contribute to a reduced displacements magnitude. Unlike Cases 1 and 2, where substantial stress variations occur, due to asymmetric heating, the simultaneous welding strategy ensures a more homogeneous thermal gradient, thereby mitigating localized stress concentrations that would otherwise promote distortions.

The findings underscore the advantages of simultaneous bilateral welding, in minimizing deformations, thereby reducing the need for post-weld corrective measures. This strategy not only enhances the geometric accuracy of the welded assembly but also lowers production costs by eliminating secondary operations, typically required to restore dimensional integrity.

4. CONCLUSIONS

The primary objective of this study was to examine the influence of welding paths on the thermal, mechanical, and displacement behaviours of T-joint configurations, applied to AA5083 aluminium alloy. Through the detailed analysis of the three proposed welding strategies (Case 1, Case 2, and Case 3), the following significant conclusions were drawn:

- The Case Study 3 reveals the most extensive HAZ width in the middle of the plate, with double size comparing to the other cases. This enlargement is attributed to the simultaneous actions of two welding heat sources that leads to greater concentration of thermal heat in that specific area.

- In Case Studies 1 and 2, the HAZ expansion in the region of the second weld seam was found to be approximately 30% larger than in the area of the first seam. This increase is a direct result of the preheating effect caused by the deposition of the initial bead, which elevates the base material temperature before the second pass, thereby promoting a broader HAZ extension.

- The analysis of the equivalent stress fields across the three case studies revealed that the maximum

stress magnitudes were relatively consistent, ranging between 170–180 MPa, with no significant variations between the three welding configurations.

- In Case Study 3, the region exhibiting maximum stress values, in the middle of the welded joint, was observed to be nearly twice higher that in Case Studies 1 and 2. This can be linked to the converging heat sources in the centre of the joint, which induce localized thermal expansion and result in larger stress-concentrated zones.

- Regarding the total displacements, Case Study 3 exhibited the lowest deformation values, with a reduction of approximately 25–30% compared to Case Studies 1 and 2. This reduction is primarily attributed to the shortened welding time required for simultaneous bead deposition, which minimizes the exposure of the welded joint to non-uniform thermal gradients. Furthermore, the more balanced stress distribution observed in Case Study 3 contributes to a uniform expansion and contraction cycle, effectively limiting overall distortions.

- For industrial applications involving AA5083 aluminium alloy It can be noticed that the simultaneous bilateral welding strategy employed in Case Study 3 proved to be the most effective in minimizing total displacements.

- Future work will focus on validating the findings of the proposed FEM analysis with respect to the industrial applications of AA5083 welding, particularly in the context of T-joint design.

REFERENCES

[1] **Gupta S., Singh D., Yadav A., Jain S., Pratap B. A.,** *Comparative Study of 5083 Aluminium Alloy and 316L Stainless Steel for Shipbuilding Material*, Materials Today: Proceedings 2020, vol. 28, pp. 2358-2363.

[2] **Hosseinabadi O. F., Khedmati M. R.,** *A Review on Ultimate Strength of Aluminium Structural Elements and Systems for Marine Applications*, Ocean Engineering, 2021, vol. 232, 109153109153.

[3] **Wahid M. A., Siddiquee A.N., Khan, Z. A.,** *Aluminum Alloys in Marine Construction: Characteristics, Application, and Problems from a Fabrication Viewpoint*. Marine Systems & Ocean Technology, 2020, vol. 15, pp. 70-80.

[4] **Iordachescu M., Iordachescu D., Planas, J., Scutelnicu E., Ocaña J. L.,** *Material Flow and Hardening at Butt Cold Welding of Aluminium*. Journal of Materials Processing Technology, 2009, vol. 209, pp. 4255-4263.

[5] **Canepa E., Stifanese R., Merotto L., Traverso P.,** *Corrosion Behaviour of Aluminium Alloys in Deep-Sea Environment: A Review and the KM3NeT Test Results*, Marine Structures, 2018, vol. 59, pp. 271-284.

[6] *** *Reference Module in Materials Science and Materials Engineering*, Hashmi, S., Ed. Elsevier, Amsterdam, vol. 2016, ISBN 978-0-12-803581-8.

[7] **Iordachescu M., Iordachescu D., Ocaña J. L., Vilaca P., Scutelnicu E.,** *FSW - Characteristic Flaws in Aluminium Alloys Joints*, Metalurgia International, 2009, vol. 14, pp. 135-138.

[8] **Sielski R. A.**, *Research Needs in Aluminum Structure∗*, Ships and Offshore Structures, 2008, vol. 3, pp. 57-65.

[9] **Çam G., İpekoğlu G.**, *Recent Developments in Joining of Aluminum Alloys*, International Journal of Advanced Manufacturing Technology 2017, vol. 91, pp. 1851-1866.

[10] **Verma R. P., Kumar Lila M. A.**, *Short Review on Aluminium Alloys and Welding in Structural Applications*, Materials Today: Proceedings 2021, vol. 46, pp. 10687-10691.

[11] **Brumm S., Bürkner G.**, *Gas Metal Arc Pulse Welding with Alternating Current for Lightweight Materials*, Materials Today: Proceedings 2015, vol. 2, pp. S179-S187.

[12] **Çam G., Mistikoglu S.**, *Recent Developments in Friction Stir Welding of Al-Alloys*, Journal of Materials Engineering and Performance, 2014, vol. 23, pp. 1936-1953.

[13] **Verma R. P., Pandey K. N., András K., Khargotra R., Singh T.**, *Difficulties and Redressal in Joining of Aluminium Alloys by GMA and GTA Welding: A Review*, Journal of Materials Research and Technology, 2023, vol. 23, pp. 2576-2586.

[14] **Çetkin E., Çelik Y. H., Temiz Ş.**, *Effect of Welding Parameters on Microstructure and Mechanical Properties of AA7075/AA5182 Alloys Joined by TIG and MIG Welding Methods*, Journal of the Brazilian Society of Mechanical Sciences, 2020, vol. 42, p. 34.

[15] **Abima C. S., Akinlabi S. A., Madushele N., Fatoba O. S., Akinlabi E. T.**, *Mechanical and Microstructural Properties of MIG Welded Aluminium Alloy*, IOP Conference Series: Materials Science and Engineering, 2021, vol. 1107, 012037.

[16] **Chen B. Q., Liu K., Xu S.**, *Recent Advances in Aluminum Welding for Marine Structures*, Journal of Marine Science and Engineering, 2024, vol. 12, 1539.

[17] **Deng D., Murakawa H.**, *Prediction of Welding Distortion and Residual Stress in a Thin Plate Butt-Welded Joint*, Computational Materials Science 2008, vol. 43, pp. 353-365.

[18] **Wang J., Yuan H., Ma N., Murakawa H.**, Recent Research on Welding Distortion Prediction in Thin Plate Fabrication by Means of Elastic FE Computation. Marine Structures 2016, vol. 47, pp. 42-59.

[19] **Yadav S., Pawar R. S., Sambare A. A., Deshpande S.**, *Finite Element Analysis and Design Optimization of Composite T-Joints for Enhanced Maritime and Aerospace Applications*, Engineering Solid Mechanics, 2024, vol. 12, pp. 157-164.

[20] **Chen Z., Liu Y., Qian H., Wang P., Liu Y.**, *Effect of Repair Welding on the Fatigue Behavior of AA6082-T6 T-Joints in Marine Structures Based on FFS and Experiments*, Ocean Engineering, 2023, vol. 281, 114676.

[21] **Churiaque C., Sánchez-Amaya J. M., Üstündağ Ö., Porrua-Lara M., Gumenyuk A., Rethmeier M.**, *Improvements of Hybrid Laser Arc Welding for Shipbuilding T-Joints with 2F Position of 8 Mm Thick Steel*, Optics & Laser Technology, 2021, vol. 143, 107284.

[22] **Hammad A., Churiaque C., Sánchez-Amaya J. M., Abdel-Nasser Y.**, *Experimental and Numerical Investigation of Hybrid Laser Arc Welding Process and the Influence of Welding Sequence on the Manufacture of Stiffened Flat Panels*, Journal of Manufacturing Processes 2021, vol. 61, pp. 527-538.

[23] **Simion G., Birsan D., Voiculescu I., Scutelnicu E.**, *Simulation by FEM of TIG Deposition Welding of Multicomponent Alloy on Carbon Steel Substrate*. Acta Technica Napocensis Series-Applied Mathematics Mechanics and Engineering, 2024, vol. 67, pp. 125-132.

[24] **Georgescu B., Simion G.**, *A Synthetic Approach to Cold Pressure Welding on Cogged Surfaces*, Annals of "Dunarea de Jos" University of Galati, Fascicle XII, Welding Equipment and Technology, 2023, vol. 34, pp. 57-64.

[25] **Chaturvedi M., Vendan Subbiah A., Simion G., Rusu C. C., Scutelnicu E.**, *Critical Review on Magnetically Impelled Arc Butt Welding: Challenges, Perspectives and Industrial Applications*, Materials, vol. 2023, vol. 16, 7054.

[26] **Lee C., Woo S., Kim, J.**, *Impact Analysis of Welding Sequence to Reduce Weld Deformation in Aluminum Hulls*, Journal of Marine Science and Engineering, 2024, vol. 12, 1604.

[27] **Jiao W., Zhao D., Yang S., Xu X., Zhang X., Li L.**, Chen, H. Real-Time Prediction of Temperature Field during Welding by Data-Mechanism Driving. Journal of Manufacturing Processes 2025, vol. 133, pp. 260-270.

[28] **Birsan D. C., Simion G., Voiculescu I., Scutelnicu E.**, *Numerical Model Developed for Thermo-Mecahnical Analysis in AlCrFeMnNiHf0.05-Armox 500 Steel Welded Joint*, Annals of "Dunarea de Jos" University of Galati, Fascicle XII, Welding Equipment and Technology, 2021, vol. 32, pp. 37-46.

[29] **Birsan D. C., Simion G.**, *Numerical Modelling of Thermo-Mechanical Effects Developed in Resistance Spot Welding of E304 Steel with Copper Interlayer*, Annals of "Dunarea de Jos" University of Galati, Fascicle XII, Welding Equipment and Technology, vol. 33, pp. 89-94.

[30] **Scutelnicu E., Iordachescu M., Rusu C. C., Mihailescu D., Ocaña J. L.**, *Metallurgical and Mechanical Characterization of Low Carbon Steel—Stainless Steel Dissimilar Joints Made by Laser Autogenous Welding*, Metals 2021, vol. 11, p. 810.